On the Detection of Flow-Induced Fractionation in Melts of Homopolymers by Normal-Mode Microdielectrometry

Jeffrey Fodor and Davide A. Hill*

Department of Chemical Engineering, University of Notre Dame, Notre Dame, Indiana 46556

Received December 10, 1991; Revised Manuscript Received March 18, 1992

ABSTRACT: A new technique is introduced that enables us to probe main-chain relaxation of polymers in the immediate vicinity of a solid surface. The method combines microdielectrometry sensors with polymers for which normal-mode relaxation can be measured dielectrically (i.e., Stockmayer's type-A polymers). The term "normal-mode microdielectrometry", or NMMD, was coined to reflect this particular combination of ingredients. The penetration depth of the electric field on a microsensor scales with the spacing between the electrode lines and can be reduced considerably by miniaturizing the device. This enables one to follow the evolution of the relaxation times of type-A polymers in an extremely localized region near the sensor surface. In this preliminary work we apply this tool to the study of flow-induced fractionation in melts of *cis*-polyisoprene undergoing plane Poiseuille-type flow. Dielectric relaxation measurements during flow startup showed the onset of a remarkable transient, consistent with the buildup of a layer of low molar mass chains near the solid surface. The real and the imaginary components of the dielectric permittivity showed both pronounced overshoots before approaching an apparent steady state. An advective mechanism could explain only the earliest stages of the transient. Upon cessation of flow, the shape and magnitude of the dielectric spectra slowly relaxed back to the equilibrium (preflow) values. The time scale of the relaxation was consistent with a reequilibration by chain diffusion of the melt composition within the dielectric control volume. A simple dielectric model of a type-A polymer mixture could qualitatively describe the general features of the data. Other possible applications of NMMD to study chain relaxation and diffusion in melts and concentrated solutions, at polymer-solid interfaces, and in polymeric liquid crystals are proposed.

Introduction and Background

Understanding the behavior of polymers near solid surfaces is of considerable technological interest. The control of adhesion of polymers[1] and tailoring polymer interfaces,[2] for instance, rely heavily on our understanding of polymer-surface interactions. Perhaps, the most intriguing fundamental questions in this area relate closely to the dynamics of polymers near a solid surface in solutions and melts undergoing flow. This problem is of great pragmatic interest, since most polymer processing operations involve flow. Many unresolved issues in viscoelastic fluid mechanics are also believed to relate to the behavior of the chains at the solid boundaries.[3]

Flow-induced segregation in polymeric liquids has attracted considerable interest lately. Segregation has indeed been observed in dilute polymer solutions[4-6] and in polymer melts blended with low molecular weight additives.[7] The notion that a polymer melt will spontaneously fractionate in flow under inhomogeneous stresses was advanced nearly 30 years ago by Busse.[8] Soon after, Schreiber and Storey[9] (see also refs 10 and 11) produced the first evidence of flow-induced fractionation in linear low-density polyethylene melts. They measured a radial gradient of molecular weight in polymer filaments extruded from a capillary die and inferred a preferential segregation of small chains at the surface. Because the analysis was done on the extrudate and not on the material in the capillary, their conclusions were tenuous. Consequently, this phenomenon has been largely overlooked by researchers in viscoelastic fluid mechanics and adhesion. Contributing to this trend may have been the lack of experimental tools to enable real-time detection of flow-induced fractionation in homopolymers.

We have devised a technique that enables us to capture experimentally flow-induced segregation in polydisperse melts of particular types of homopolymers. Our method combines two well-established tools: (1) dielectric spectroscopy and (2) modern microelectronic devices. Dielectric relaxation has earned great popularity over the years,[12,13] thanks primarily to its versatility and accuracy. Specimen clarity is not required, making this method very attractive. The technique has been employed to monitor the cure of thermosets,[14-17] to study phase transitions in amorphous, crystalline, and liquid crystalline polymers,[12,18-25] and to probe chain motion in semiflexible rodlike polymers in solution[26-28] and in biopolymers.[29]

For polymers having one of the components of the segmental dipole moments aligned head-to-tail along the backbone, the global dipole moment is proportional to the end-to-end vector of the chain. Such polymers were classified as type-A chains by Stockmayer,[30] and this terminology will be adopted here as well. *cis*-Polyisoprene is a flexible polymer showing this property.[31-36] For these materials the dielectric-loss spectrum shows distinct "segmental" and "normal-mode" peaks. A segmental peak stems from relaxation of the components of the segmental dipole moments perpendicular to the chain contour and thus reflects motion of subchains of only a few monomers. Therefore, the position in frequency space of the peak is independent of polymer molecular weight.[32-36] Conversely, normal-mode relaxation involves coordinated motion of the entire chain, leading to a characteristic frequency which depends strongly on the chain length. For these systems a very close analogy between dielectric and rheological relaxation can be tied.[35] In flexible type-A polymers the dielectric normal-mode and the viscoelastic relaxation times show approximately the same 3.5 (±0.2) power-law dependence on molecular weight.[35,37-39] Dielectric measurements can then provide information on the rheology and, thus, indirectly, on the molecular weight of a sample.

Modern photolithography enables fabrication of dielectric sensors (small capacitors) that can probe regions only a few microns deep (measured from the surface of the sensor). Therefore, by "seeding" miniaturized sensors at the boundaries of a flow and using type-A polymers, it is possible not only to monitor the extent of flow-induced

0024-9297/92/2225-3511$03.00/0

segregation in homopolymers but also to obtain information on the molecular weight of the segregated species. Furthermore, the sensor can be designed to produce anisotropic electric fields. This enables us additionally to detect anisotropy in the dielectric permittivity of the material, giving details about the local orientation of the chains.

To summarize, our technique makes use of (1) dielectric spectroscopy with miniaturized sensors and (2) polymers for which normal-mode relaxation can be measured dielectrically (i.e., coillike or rodlike macrodipoles). The term "normal-mode microdielectrometry", or NMMD, was coined to reflect this particular combination of ingredients. The method can provide information on (1) the extent of segregation, (2) the relaxation time (and, indirectly, the molecular weight) of the segregated material, and (3) the degree of molecular anisotropy. This technique holds promise for analysis of opaque liquid crystal polymers also, since it does not demand transparent samples. Indeed, most liquid crystals possess large dielectric anisotropies, and this method should be ideal. Segregation of additives from polymer melts undergoing flow can also be studied in this way. However, information on full-chain relaxation can be obtained only for type-A polymers.

In this paper we present results of dielectric relaxation experiments performed on a flowing *cis*-polyisoprene (*cis*-PI) melt. As mentioned above, *cis*-PI has a large dipole moment parallel to the end-to-end vector of the chain, which makes it an ideal candidate for our studies. Also, the rheological properties and the dielectric behavior of the material in the quiescent state have been well documented in the literature.[31-36] Furthermore, our samples are liquid at room temperature, and this facilitates substantially the experiments (relative to high melting-point polymers). We have used planar interdigitated-combs sensors to measure the near-wall ($\sim 10\ \mu$m) dielectric properties of the melt in plane Poiseuille-type flow. This flow geometry is ideal for three reasons: (1) it is simple to produce, (2) it is common in processing operations, and (3) it produces a well-characterized shear stress profile across the flow gap. We have performed inception-of-flow and relaxation-after-flow experiments. In both cases the evidence points consistently to flow-induced segregation of low molecular weight species at the boundaries. The main qualitative features of our data can be rationalized based on a simple dielectric model of a polydisperse mixture.

This paper is organized as follows. We discuss first details about the dielectric sensor and apparatus. To maintain focus on the results, theoretical considerations about the description of the electric field on the sensor have been confined to an appendix. Next, we describe the flow cell. A section devoted to the rheological and (static) dielectric characterization of our samples follows. We then present experimental results of inception-of-flow and relaxation-after-flow experiments. The results are interpreted and discussed in an appropriate section. Finally, we propose other possible applications of this technique to probe chain relaxation dynamics in polymer solutions and melts and at polymer–nonpolymer interfaces.

Experimental Methods

Dielectric Sensor. A microfabricated dielectric sensor is a capacitor consisting of a periodic pattern of interdigitated metal lines deposited on a flat substrate.[16] We have designed and produced (through Thin Film Technology, Buellton, CA) sensors of two different sizes. Scanning electron micrographs of one of the smaller chips at various levels of resolution are given in Figures 1 and 2. Evenly spaced gold lines, of equal width and spacing, have been deposited by photolithography on fused silica substrates. All sensors have approximately 160 lines, regardless of size. The smaller capacitors (Figures 1 and 2) have lines 12.5 μm wide, 3.5 mm long, and 5 μm thick, while in the larger chips the lines are 25 μm wide, 7 mm long, and 2 μm thick. The line aspect ratio, equal for all sensors, is around 280. Therefore, the electric field is nearly two-dimensional. In the present study the larger sensors only were used.

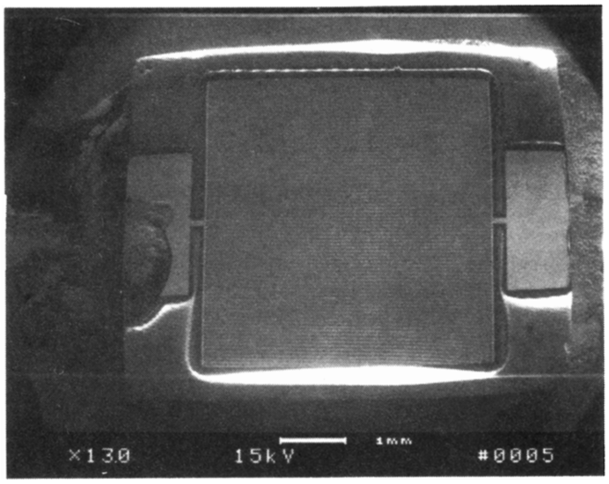

Figure 1. Scanning electron micrograph giving a global view of one of our small sensors. The pattern of gold lines, barley visible at this magnification, can be more distinctly recognized in Figure 2. The two large rectangular areas on the left and right of the comb pattern are connection pads.

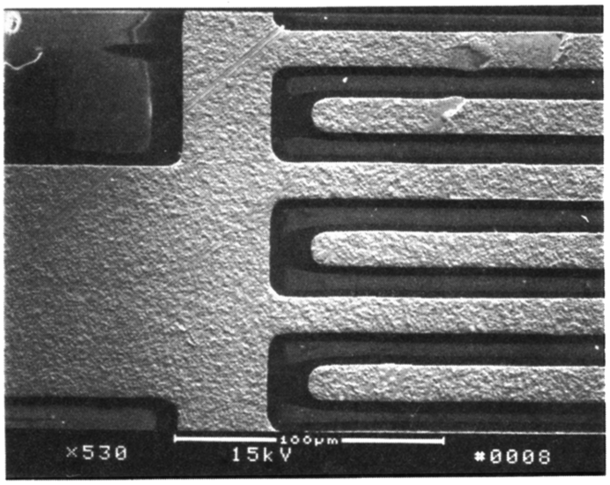

Figure 2. Higher resolution scanning electron micrograph of the dielectric sensor in Figure 1. The interdigitated pattern is clearly visible here.

Our microcapacitors are similar to, but simpler than, conventional microdielectrometry sensors.[14-16] (Commercial sensors are typically patterned on either silicon or a polymer substrate. The intrinsic dielectric response of these materials can complicate signal analysis. Fused silica has a simpler response.) Planar interdigitated-combs sensors are not new and are now routinely employed for characterization of polymers. One of the most common applications is monitoring of the cure of thermosetting resins.[14-17] Despite the widespread use of these sensors, the potential of the interdigitated-combs geometry to perform extremely localized and "polarized" (see below) relaxation measurements in type-A polymers has never been previously recognized.

Due to the nearly two-dimensional and periodic geometry of the electrodes, the electric field on the chip is itself two-dimensional and periodic. The field is perpendicular to the lines, i.e., it is strongly directional, and thus polarized. This is schematically illustrated in Figure 3. The periodic line pattern imparts to the field a finite "penetration depth", comparable in magnitude to the spacing between the lines. (This can be easily

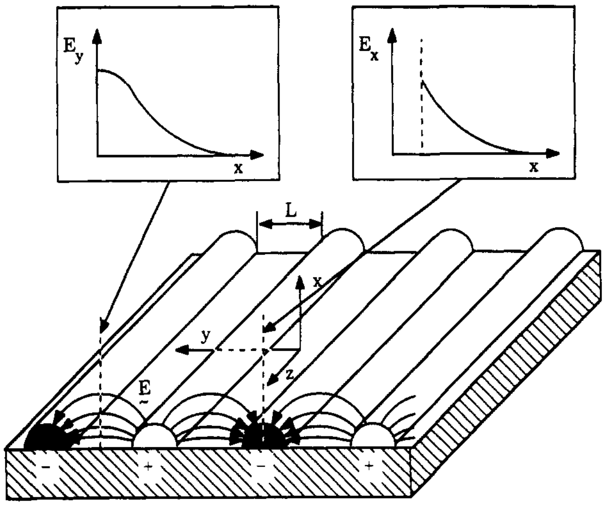

Figure 3. Schematic view of the interdigitated electrodes. The curves between the electrodes of opposite polarity are the stream lines of the electric field, E, which is two-dimensional and periodic. The top graphs illustrate schematically the decay of E_x and E_y, at the selected locations, where they achieve their maxima. At large distances ($x > L/\pi$) the field decays exponentially. Due to this strong localization the device capacitance is highly susceptible to changes within the pervaded volume but insensitive to remote external disturbances.

calculated by assuming the lines to be 2D sources and sinks and by using the analogy between potential flow and electrostatics. The solution to this problem, which is almost entirely available in classical fluid mechanics textbooks,[40] is outlined in the appendix.) It is this strong localization of the field that enables one to selectively probe regions very close to the solid boundary.

Oscillatory dielectric measurements yield a complex impedance vector, with real and imaginary components which are direct functions of the resistivity and dielectric constant of the material. Our raw data could satisfactorily be described by a conventional equivalent circuit of capacitors and resistors in parallel.[12,13] For this model, the measured capacitance and the reciprocal of the product of the resistance by the frequency are linear combinations (through a set of instrumental constants) of the real, ϵ', and imaginary, ϵ'', components of the dielectric permittivity of the fused silica substrate and the polymer. Therefore, the instrument can be calibrated based on the response of the "blank" chip. (Due to the large surface-to-volume ratio of the sensor, great care and many precautions are required to avoid contamination of the active area, the penalty being irreproducible measurements.)

Dielectric measurements were carried out with an HP 4284A impedance analyzer. The voltage and frequency ranges of the instrument are 5 mV to 2 V (peak-to-peak), and 20 Hz to 1 MHz, respectively, with a basic accuracy of 0.05% and a nominal resolution of 10^{-4} pF. For given acquisition time and voltage the accuracy varies greatly with the frequency. In the experiments described below, a voltage of 100 mV was used, resulting in a reproducibility of about 1% above 1 kHz. Because of the strong frequency dependence of the error below 1 kHz, in the following plots of the loss spectra will also show a curve representative of the 95% confidence error.

Description of the Flow Cell. Dielectric measurements on the flowing polymer were taken in a custom-designed plane Poiseuille-type flow cell. Plane Poiseuille flow is characterized by a linear shear stress profile across the channel, symmetric about the centerline of the gap between plates, where the shear stress vanishes. The shear stress at the wall and the profile are independent of the rheology of the material and depend only on the imposed pressure drop and channel geometry. Therefore a nonuniform but well-characterized stress field is produced in this system. A schematic of the flow cell is given in Figure 4. The cell is carved from a solid block of aluminum, to minimize compliance under pressure. The polymer flows from a nitrogen-pressurized reservoir into the cell through an inlet port. After the port and prior to entering the control channel, there is a small equilibration cavity. The remainder of the flow geometry is the mirror-image of the inlet. The entry and exit regions of the control channel are tapered on one side by 21° from the channel walls. The microsensor is centered within the channel and mounted flush to the wall opposite to the tapered surface. There is no restriction to the orientation of the chip relative to the flow. In the experiments below the lines were set parallel to the flow, and the electric field was perpendicular to the fluid velocity. (In this configuration, chain stretching and reorientation in the direction of the flow would decrease the component of the dipole moment parallel to the field and, consequently, decrease the dielectric constant.) The top of the cell, which houses the chip and defines one of the boundaries of the channel, can be readily unbolted from the bottom. The channel is 2 cm wide and 2 cm long, and the flow gap is controlled by means of spacers. In the experiments below the gap was set to 250 μm. With this gap, the pressure drop in the control channel is about 80% of the total, based on a Newtonian estimate. The entire cell can be statically pressurized to calibrate for possible variations of sensor capacitance with changes in the geometry. Preliminary experiments have revealed only a very small influence of the hydrostatic pressure on the impedance of the polymer-filled flow cell. These effects were later proven to be irrelevant compared to the ones brought about by flow.

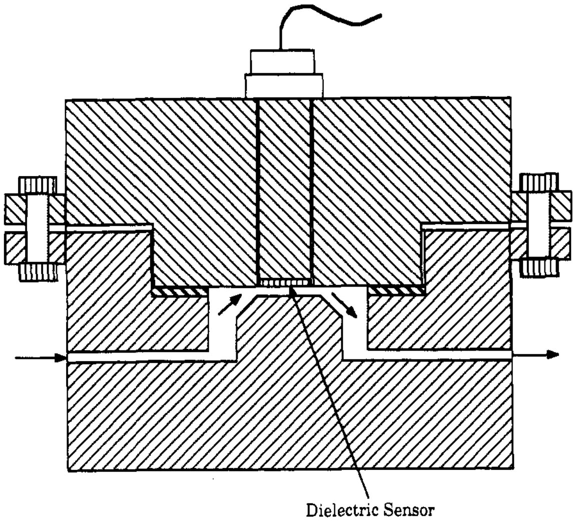

Figure 4. Schematic of the plane Poiseuille flow cell. The sensor is flush-mounted to the top wall with the lines parallel to the flow.

Materials. A commercial sample of liquid *cis*-polyisoprene (*cis*-PI; Kuraray Co., Ltd., Japan) of 29 000 viscosity-averaged molecular weight and a polydispersity index close to 2 was used (these data were provided by the manufacturer). The polymer had a reported a content of 0.10 wt % of BHT (2,6-di-*tert*-butyl-4-methylphenol) antioxidant and 0.50 wt % volatiles (the latter comprising light hydrocarbons, unreacted monomer, and oligomers). It was stored at room temperature in sealed polypropylene bottles and was used as recieved. Information on the cis/trans ratio was not available. We have compared dielectric and rheological spectra, and we have found that the corresponding normal-mode relaxation times are indeed comparable (see the section on material characterization). This finding can be explained only in terms of a reasonably large cis/trans ratio.[34]

Results

Rheological Characterization. The polymer was characterized rheologically by small amplitude (30% maximum strain) oscillations at frequencies between 0.01 and 10 Hz in a cone-and-plate controlled-stress rheometer (CARRI-MED CSL). The cone angle and diameter were 2° and 4 cm, respectively, and the temperature ranged between 0 and 50 °C. For measurements between 23 and 50 °C the cone-and-plate volume was filled completely. At lower temperatures, between 0 and 15 °C, accurate strain measurements could not be taken with full sample volumes, due to the coupling of the large viscosity of the material with torque limitations of our instrument (maximum torque = 10^{-2} Nm). Therefore, only a fraction of the total volume was used. The diameter of the circular wetted-area, *d*, was determined a posteriori with a micrometer, and the viscosities were then corrected by multiplying by the factor $(4/d)$.[3] The accuracy of this procedure was verified independently by two different methods. The viscosity of the material at 30 and 50 °C was measured first with a reduced sample size and corrected a posteriori for wetted-area differences. These viscosities were then compared to the ones obtained at the same temperatures but with full sample volumes. Alternatively, reduced samples were run repeatedly at 50 °C and at the low temperature of interest (this required readjustment of the rheometer gap, which may have introduced uncertainties). The geometrical scale factor was then calculated from the ratio of the apparent viscosities of the full to the reduced samples, at 50 °C. Overall both procedures gave an agreement of 5%.

Time–temperature superposition was found to be applicable, and the temperature dependence of the zero-shear viscosity, η_0, could be described within 1% by the following Vogel–Fulcher–Tamman-type correlation:[41-43]

$$\eta_0(T) = 0.0118 \exp\left(\frac{1121.2}{(T - 176.06)}\right); \quad \eta_0 \equiv (\mathrm{Pa\ s}),\ T \equiv (\mathrm{K}) \tag{1}$$

The exponential parameters are in good agreement with published values.[32-36]

The measured real components, η', of the complex viscosity, normalized by their zero-shear limit, satisfactorily superposed onto a master curve when plotted against the reduced frequency

$$f \cdot \left(\frac{\eta_0(T)\ (273.16)}{\eta_0(0\ °\mathrm{C})\ T}\right) \tag{2}$$

where *f* is the frequency in hertz, and *T* is in Kelvin. Note that the frequency shift factor in eq 2 refers to 0 °C. The master curve is given in Figure 5 together with a fit of the 0 °C data. The fit assumes the model

$$\frac{\eta'(f)}{\eta'_0} = \frac{1}{(1 + (f/f^*)^n)} \tag{3}$$

where f^* and *n* are adjustable parameters. The values $n = 1.51$ and $f^* = 37$ Hz (at 0 °C) were determined by linear regression of the data transformed as follows:

$$\log\,(\eta'_0/\eta' - 1) = n \log\,(f) - n \log\,(f^*) \tag{4}$$

A plot of this relation and the data is given in Figure 6. The fit is reasonable, in view of the small departure of the viscosities from the low-frequency asymptote. The power-law exponent $n = 1.51$ also agrees reasonably with the theoretical value of 2 expected for monodisperse polymers.[37-39] From the threshold frequency $f^* = 37$ Hz and the relation $\lambda = (2\pi f^*)^{-1}$, an estimate of the relaxation time of the polymer, $\lambda(0\ °\mathrm{C})$, can be obtained. We calculated $\lambda(0\ °\mathrm{C}) = 4.3 \times 10^{-3}$ s. An independent estimate of λ can also be calculated from the zero-shear viscosity and the plateau shear modulus, G_p, as follows:[37-39] $\lambda = (12/\pi^2)\eta_0/G_p$. We were unable to measure G_p of our polymer. Adachi and co-workers[35] measured G' and G'' of *cis*-PI melts of narrow molecular weight distribution at 273 K, and they were able to reach the plateau. G_p is insensitive to the details of the molecular weight distribution of the polymer; therefore, we can use their value to estimate the relaxation time of our sample with our value of the viscosity $\eta_0(0\ °\mathrm{C}) = 1.22 \times 10^3$ Pa s. From Figure 8 in ref 35 we estimated $G_p \sim 0.4$ MPa, giving $\lambda(0\ °\mathrm{C}) = 3.77 \times 10^{-3}$ s. This is in reasonable agreement with $\lambda(0\ °\mathrm{C}) = 4.3 \times 10^{-3}$ s determined from the viscosity master curve. With these values and knowledge of the temperature dependence of the viscoelastic shift factor, the relaxation time at any other temperature can be determined.

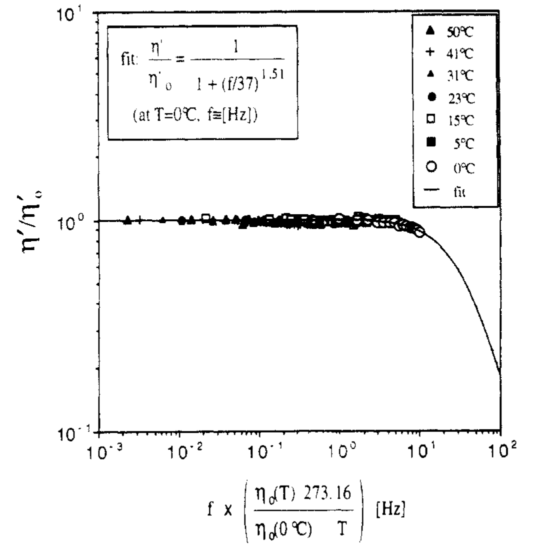

Figure 5. Master curve of the normalized real component of the complex viscosity versus reduced frequency. The viscosities were normalized by their zero-shear limit, and the frequency shift factor refers to 0 °C. The frequency, *f*, is given in hertz. Also shown is the fit of the 0 °C data according to the equation given at the top left corner of the figure.

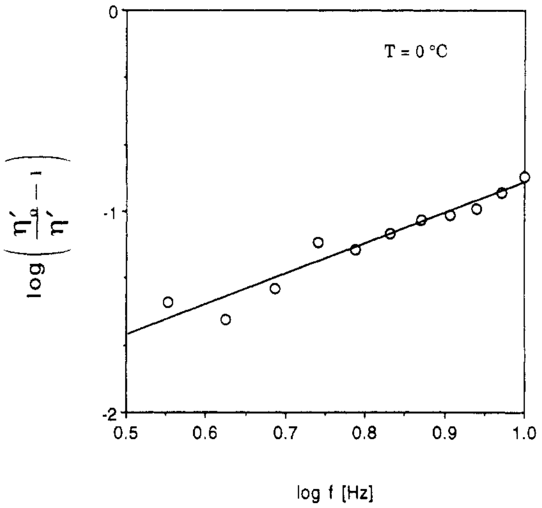

Figure 6. Logarithmic plot of the 0 °C viscosity versus frequency data transformed according to eq 4. The line is the best power-law fit.

Dielectric Characterization. The polymer was tested dielectrically at rest. A thermostated and electrically shielded cell was used to test the material on the chip between 30 and 80 °C. Time–temperature superposition was applicable to these dielectric data also. The ϵ'' spectra were normalized by their peak values and shifted horizontally to match the 80 °C data, giving the master curve shown in Figure 7. A parallel-plate fixture was also used (at 25 °C) to verify independently the performance of the chip, and these data are also given in Figure 7. The sensor and parallel-plate results are in good agreement. The ϵ'' spectra from the sensor were obtained by subtraction of the calibration spectra (determined a priori at the selected temperatures with the clean sensor) from those of the *cis*-PI + chip. The parallel-plate data did not require any correction. The intrinsic dielectric loss of the sensor was

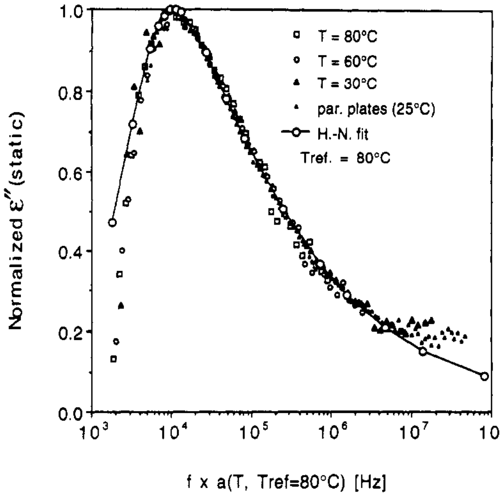

Figure 7. Master curve of the dielectric loss of *cis*-polyisoprene, ϵ'', versus reduced frequency. The original spectra were normalized by their peak values and shifted horizontally to match the 80 °C spectrum. The open circles, squares, and triangles are the sensor (chip) data at the noted temperatures, while the filled triangles are the parallel-plate results at 25 °C. The large open circles connected by the solid line represent the Havriliak–Negami fit.

small relative to that of the polymer but reproducibility of conditions in the separate measurements was crucial to these experiments. Furthermore, the frequency shift factors were calculated based on the normal-mode process, which is known to have a slightly different temperature dependence from the segmental process.[36] Indeed, the scatter in Figure 7 becomes appreciable especially at high frequencies, where the curves show an upturn indicative of the approach to a segmental peak.

Shown in Figure 7 is also a fit according to the Havriliak–Negami (HN) function[44,45]

$$\tilde{\epsilon}_{\mathrm{HN}} = \epsilon_\infty + \Delta\epsilon^*(1 + (j\omega\lambda_{\mathrm{HN}})^{\xi})^{-\mu} \tag{5}$$

where ϵ_∞ is the limiting high-frequency permittivity, $\Delta\epsilon^*$ is the relaxation strength, $j^2 = -1$, ω is the frequency, λ_{HN} is the relaxation time, and ξ and μ are parameters. The values of the parameters were determined to be $\xi = 1.0$, $\mu = 0.30$, and $\lambda_{\mathrm{HN}} = 3.98 \times 10^{-5}$ s (at 80 °C). The relatively low value of exponent μ is consistent with the polydispersity of the sample.[34]

Note that the normal-mode peak in Figure 7 occurs around 10 kHz (at 80 °C), giving a relaxation time $\lambda_{\mathrm{peak}} = 1.59 \times 10^{-5}$ s (at 80 °C). On the other hand, the HN relaxation times is $\lambda_{\mathrm{HN}} = 3.98 \times 10^{-5}$ s (at 80 °C), i.e., about a factor of 2.5 higher. This sets an uncertainty on the value to be chosen for comparison with the viscoelastic measurements. Therefore, in the following both values will be used.

Figure 8 combines the dielectric and viscoelastic shift factors, $a(T)$, normalized to give $a(30\ °\mathrm{C}) = 1$. Shown in the figure are also the dielectric shift factors of Imanishi and co-workers[34] for polyisoprenes of different molar masses (these data were normalized also). All data collapse onto a single curve, thus confirming correlation between dielectric and rheological measurements. Comparison of dielectric and viscoelastic relaxation times should further substantiate this hypothesis. Because time–temperature superposition is applicable, the dielectric relaxation time at 0 °C can be obtained from that at 80 °C by multiplying the latter by the factor $(a(0\ °\mathrm{C})(353)/(a(80\ °\mathrm{C})(273))) = 284$. We obtain $\lambda_{\text{diel-peak}} = 4.5 \times 10^{-3}$ s and $\lambda_{\text{diel-HN}} = 1.13 \times 10^{-2}$ s. Zimm's theory, for chains with hydrodynamic interactions, predicts that for monodisperse type-A polymers the following relation should hold: $\lambda_{\mathrm{diel}} = 2\lambda_{\mathrm{ve}}$.[46] Therefore, from the viscoelastic measurements we obtain $\lambda_{\mathrm{diel}} = 8.6 \times 10^{-3}$ s, which is intermediate between the values given above (the deviation between the average of the dielectric values and the viscoelastic prediction is about 8%). Possible causes for this discrepancy may be (1) inaccuracies in our procedure to estimate λ_{ve}, (2) sample polydispersity, and (3) nonoptimal cis/trans ratio. We are unable at this point to conclusively rule in favor of any of the above causes. Given the polydispersity of our sample, we believe that even the finding $\lambda_{\mathrm{diel}} = \lambda_{\mathrm{ve}}$ would not be unreasonable. This minor discrepancy is certainly acceptable within the context of this work, which aims primarily at establishing the validity of our technique.

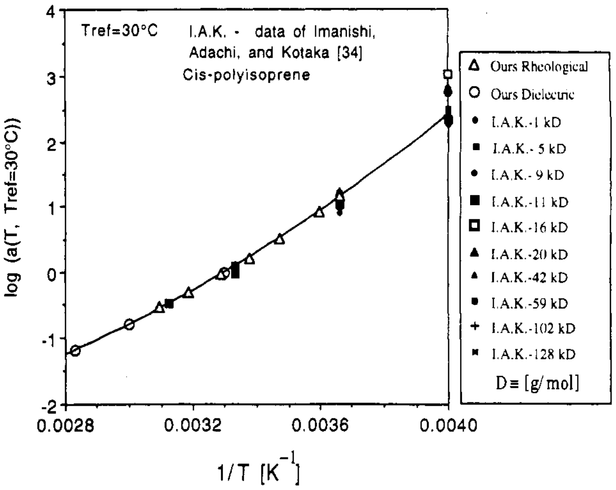

Figure 8. Dielectric and viscoelastic shift factors from the present work ("Ours") and from the dielectric data of Imanishi, Adachi, and Kotaka (I.A.K.).[34] All shifts have been normalized to give $a(30\ °\mathrm{C}) = 1$.

Dielectric Measurements on the Flowing Polymer. Inception of Flow Experiments. We obtained evidence of (what we believe to be) flow-induced fractionation in our *cis*-PI samples by performing in sequence start-up and relaxation experiments.

The experiments were all run at room temperature (24 °C). The flow cell was first filled with polymer by subjecting it to a high vacuum on one end. This procedure ensured the absence of air bubbles in the flow system and at the sensor surface. The system was allowed to relax for about a day. The cell was then statically pressurized to calibrate for pressure effects. Flow was initiated by opening the exit port of the cell, and the pressure drop was set at 0.14 MPa. The dielectric properties of the polymer in flow were measured at a frequency of 1 kHz and an applied peak-to-peak voltage of 100 mV. (Under this voltage a field of 40 V/cm develops between electrodes spaced 25 μm apart. This field is too small to influence sensibly the orientation of the polymer molecules.)

As shown in Figure 9, a remarkable transient developed. Note that the figure spans a time scale of about 2 h, while the polymer relaxation time was determined rheologically (and dielectrically) to be about 0.46 ms (at 25 °C). Therefore, the transient cannot be attributed to viscoelastic relaxation. ϵ' and ϵ'' both underwent long transients. The two functions mimicked each other closely, and thus in Figure 9 we have only reported ϵ'. (The data have been normalized by their value at inception of flow. The small decrease at the beginning of the curve (for $t < 0$) represents relaxation from the cell-loading history. The reasons for this relaxation will become clear below. The flow started at the minimum of the curve.) In Figure 9 we have also reported results of an experiment performed under a

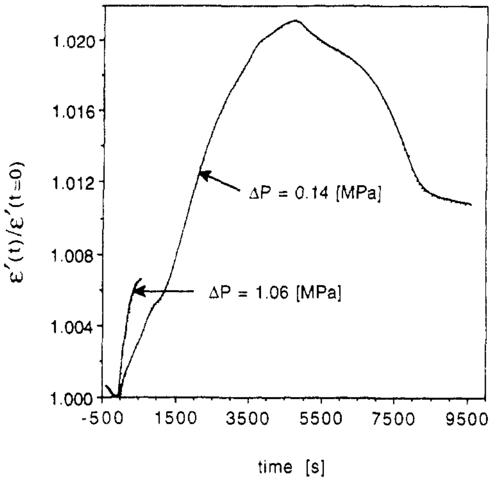

Figure 9. Plots of the real component of the dielectric permittivity of *cis*-PI, ϵ', against time (in seconds) for the inception-of-flow transients. ϵ' was normalized by the value at $t = 0$. The data were gathered at 1 kHz, 25 °C, and at the noted values of the pressure drop. The experiment at 1.06 MPa was terminated due to an insufficient amount of polymer in the reservoir.

constant pressure drop of 1.06 MPa. Note that the initial slopes of the curves increase with increasing ΔP and that the top curve shows a pronounced overshoot before the final approach to an apparent steady state. (The experiment at 1.06 MPa was terminated due to an insufficient amount of polymer in the reservoir.)

Relaxation after Flow. The experiment at 0.14 MPa was continued to test the behavior of the polymer after cessation of flow. Once the signal had reached an apparently steady value (the achievement of a steady state is not essential to the following discussion), the flow was stopped by depressurizing the cell, and the exit port was tightly capped to avoid further flow. Dielectric spectra were acquired at various times thereafter. There were no sudden variations in the dielectric constant (which could have perhaps indicated strain-induced dielectric anisotropy), but in fact it took 4 days for the signal to drop back to the original preflow values.

Figure 10 shows the dielectric spectra at various times during the relaxation transient. The curves have been normalized by the peak loss of the top spectrum. In addition to the calibration correction, the spectra were also corrected by subtracting off a segmental contribution, ϵ''_s. The functional form of ϵ''_s was selected based on the results of Boese and Kremer.[36] They found that the complex dielectric permittivity of the segmental process, ϵ_s, could be described by the HN function[44,45] (see eq 5) and reported the following values for the segmental exponents: $\xi = 0.70$ and $\mu = 0.5$.[36] For $\omega\lambda_s \ll 1$ (λ_s = segmental relaxation time) eq 5 can be simplified to give a dielectric loss of the form: $\epsilon''_s = kf^{0.70}$, where f is the frequency in hertz. This approximation was reasonable in our case, since λ_s is on the order of 10^{-8} s, at 25 °C. The value of parameter $k = 4.61 \times 10^{-6}$ Hz$^{-0.7}$ was chosen so as to linearize the high-frequency region of the normalized spectra on a log–log scale, while preserving the continuity of the slope. (Note that the reported value of k has also been scaled by the peak loss of the top spectrum of Figure 10.)

Superposed to the long-time spectrum (4 days) in Figure 10 is the HN fit (solid line) of the quiescent data of Figure 7 (shifted to 25 °C). The fit and the data are in good agreement (the percent error is plotted at the bottom of the figure). The top solid line is again the fit of the 4-day data but shifted upward to match the peak of the top spectrum. It is evident that the curves have undergone not only a vertical shift but also a change in shape.

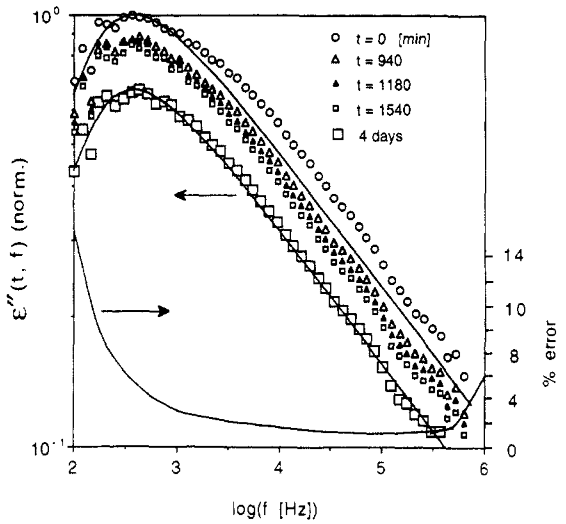

Figure 10. Loss spectra at various times following cessation of flow. All curves were normalized by the peak loss of the top spectrum. The solid line through the 4-day data is the HN fit of the quiescent spectra of Figure 7. The top solid line is identical to the previous one but has been shifted upward to match the peak loss of the top spectrum. The curve at the bottom of the figure is the frequency-dependent percent error.

Shape and magnitude changes in the spectra can simultaneously be evidenced by plotting the dielectric loss at the running time versus that at long times. These plots are given in Figure 11. In the absence of distortion the data should have followed a straight line with only an increased slope (due to the vertical shift in Figure 10). The unrelaxed data, however, show also a pronounced curvature in the central region. Because the loss spectra are monotonic above 1 kHz, the curvature in Figure 11 maps into a bulge in the spectra in the midfrequency range, thus reflecting an increased population of fast-relaxing species near the wall. Note that while the slope relaxes back slowly to unity (i.e., to the "identity line", representative of the long-time spectrum), the curvature fades away on a much faster time scale. This suggests that it should be possible to represent the data in Figure 10 by a linear combination of the long-time spectrum plus an "excess" spectrum, each weighed by an appropriate time-dependent coefficient. Therefore, we assume the functionality

$$\epsilon''(t,\omega) = \alpha(t)\, \epsilon''(t \rightarrow \infty,\omega) + \beta(t)\, \epsilon''^{*}(t,\omega) \qquad (6)$$

where $\alpha(t)$ and $\beta(t)$ are time-dependent coefficients, $\epsilon''(t \rightarrow \infty,\omega)$ is the long-time spectrum, and $\epsilon''^{*}(t,\omega)$ is an excess spectrum. The time dependence in ϵ''^{*} has been included to account for possible variations of the relaxation time of this component. Note that, at long times, the spectra relax back to the equilibrium curve; thus, we expect $\alpha(t \rightarrow \infty) = 1$ and $\beta(t \rightarrow \infty) = 0$.

In order to calculate the coefficient $\alpha(t)$, we note that there is no shift of the peak frequency of the loss maxima in Figure 10 with time. This indicates that the second term on the right-hand side of eq 6 is negligible in that frequency range. Therefore, $\alpha(t)$ can be obtained from the ratio of the peak losses of the transient to the long-time spectrum. The function $\beta(t)\, \epsilon''(t,\omega)$ can then be calculated by subtraction according to eq 6. The results of these calculations are shown in Figures 12 and 13.

Figure 12 gives the excess spectra (i.e., function $\beta(t)\, \epsilon''(t,\omega)$) plotted against frequency and parametrized in time. As mentioned above, these curves should represent

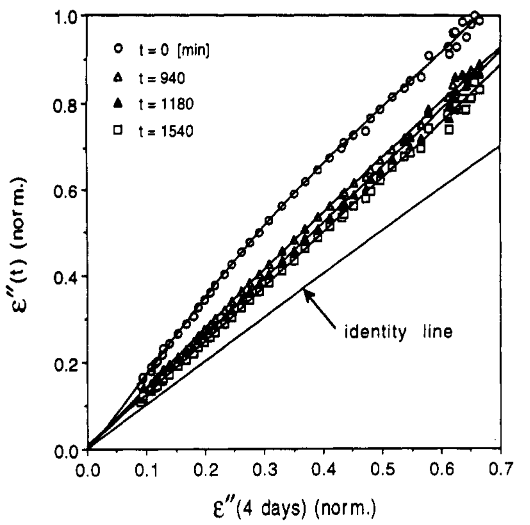

Figure 11. Plot of the dielectric loss following cessation of flow versus that at long times. Note the pronounced curvature in the top data.

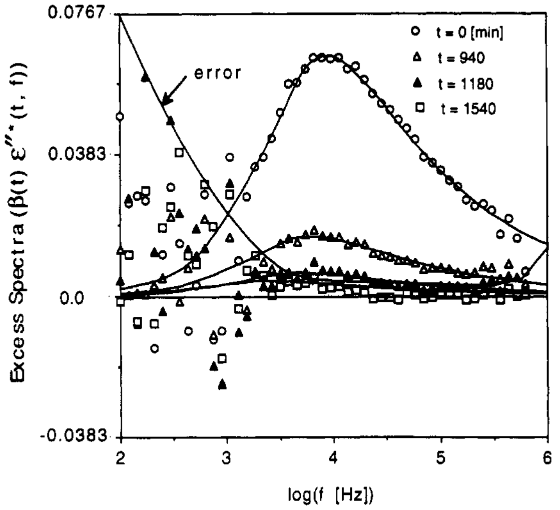

Figure 12. Plot of the excess spectra $\beta(t)\ \epsilon''^*(t,f)$. The curve on the left is the absolute error bar, which can be read off directly from the ordinate scale.

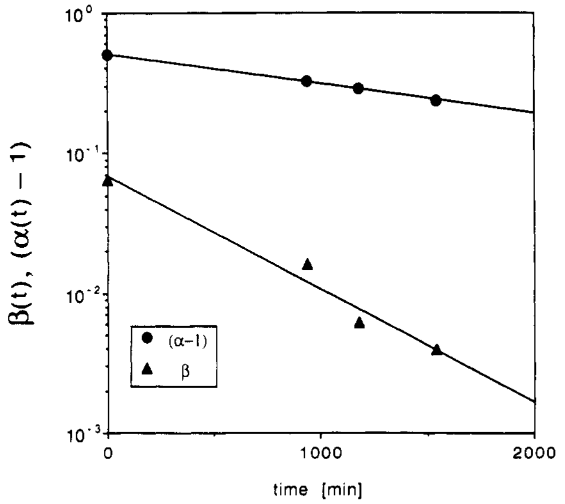

Figure 13. Semilogarithmic plots of the experimental functions $\beta(t)$ and $\alpha(t) - 1$. $\beta(t)$ represents the height of the loss peaks in Figure 12 and has been calculated by imposing $(\epsilon''^*)_{\text{peak}} = 1$.

the spectra of the fast-relaxing species. A peak at about 9 kHz has emerged. The peak is very strong at $t = 0$ (when the flow was terminated) and gradually disappears in time. There is a shift of the maximum to the left with increasing time, indicating the gradual replacement of small chains (with small relaxation time and larger diffusivity) with longer ones. The solid lines through the data are Havriliak–Negami fits, according to eq 5. The fit parameters are listed in Table I. It is worth noticing that the exponents $\xi = 1$ and $\mu = 0.40$ are virtually identical to those of the normal-mode process reported by Boese and Kremer.[36] This finding lends credence to the spectrum decomposition procedure outlined in eq 6.

Table I
Havriliak–Negami Parameters for the Excess Spectra ($\beta(t)\epsilon''^*(t, \omega)$)

time (min)	ξ	μ	$\beta(t)^{a,b}$	λ_{HN} (μs)
0	1.0	0.40	6.48×10^{-2}	39.8
940	1.0	0.40	1.61×10^{-2}	56.2
1180	~1.0	~0.40	6.14×10^{-3}	~71
1540	~1.0	~0.40	3.91×10^{-3}	~140

[a] Referred to the peak loss of the top spectrum in Figure 10. [b] Note that we have assumed $(\epsilon''^*)_{\text{peak}} = 1$.

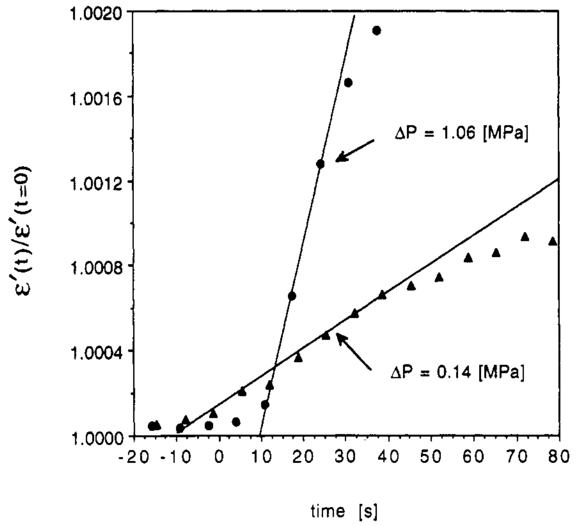

Figure 14. Short-time behavior of the data in Figure 9. The lines are the best fits. The slopes are in a ratio of 6.7.

Below 1 kHz the noise in Figure 12 increases sharply, due to the smaller number of sample averages allowed for a given acquisition time. This effect is quantified by the error-bar curve, drawn at the 95% confidence level.

From the peak loss of the spectra in Figure 12 the coefficient $\beta(t)$ in eq 6 can be calculated. These values are also reported in Table I. (Note that we have assumed $(\epsilon''^*)_{\text{peak}} = 1$.) Figure 13 gives semilog plots of $\alpha(t) - 1$ and $\beta(t)$ with exponential fits. The separation in time scales between relaxation of the slope and curvature in Figure 11 clearly emerges here. The rationale for our choice of exponential fits is explained below.

Discussion

The initial slopes of the curves in Figure 9 increased with pressure drop. A mechanism based on advection of small chains to the wall could explain this observation, since diffusivities of polymer chains in the melt are small (typically 10^{-11}–10^{-13} cm^2/s). At 1.06 MPa the wall shear stress was about 5.3 kPa. With a zero-shear viscosity of 116 Pa s and a relaxation time of 4.6×10^{-4} s (at 25 °C), we estimated a Deborah number of 2×10^{-2}, indicating that the polymer was essentially Newtonian. The slope increase can then be directly related to an increase in the flow rate (assuming homogeneity of flow). Figure 14 expands the short-time behavior of the signal and gives linear fits of the data. The ratio of the experimental slopes is 6.7, which agrees reasonably with the value of 7.5 obtained from the pressure drops.

The data at 0.14 MPa in Figure 9 show a pronounced overshoot. The reason for this phenomenon are unclear at the moment, but we speculate that it may be due to a transient redistribution of the species near the surface. If the abundance of low molar mass species at the surface increases in time, then the average relaxation time of the surface material will decrease. This will be reflected in both a growth and a shift to the right of the excess peak (i.e., the reverse of what is observed in Figure 12). A scenario is possible whereby the growth and shift to higher frequencies of the excess peak progress with different time scales. In other words, the peak grows first and then gradually shifts to the right (while continuing to grow). When monitored at a constant frequency this effect would show up as an overshoot, as observed in Figure 9. Experiments are in progress to test this hypothesis.

The upward shift of the spectrum in Figure 10 can be rationalized based on a simple model of a mixture of two homopolymers with widely separated normal-mode relaxation times. A wide separation of relaxation times can easily be achieved in a melt, even with modest differences of molecular weight. In the simplest case, the dielectric function of this system takes on the form[33]

$$\Delta\tilde{\epsilon} = \frac{\xi_{\mathrm{n}}}{kT}(n_1{\mu_1}^2 f_1(j\omega\lambda_1) + n_2{\mu_2}^2 f_2(j\omega\lambda_2)) + (n_1X_1 + n_2X_2)\frac{\xi_{\mathrm{s}}{\mu_{\mathrm{s}}}^2}{kT}g(j\omega\lambda_{\mathrm{s}}) \quad (7)$$

where $\Delta\tilde{\epsilon}$ is the increment of the dielectric constant over the infinite-frequency value, ξ_{n} and ξ_{s} are constants (n = normal mode, s = segmental), kT is the Boltzmann temperature, ω the frequency of the electric field, $j^2 = -1$, and n_i, μ_i, λ_i, and X_i are the molar density, dipole moment, relaxation time, and molar mass of species i (i = 1, 2, s), respectively. Note that $\Delta\tilde{\epsilon}$ has been separated in two contributions. The first term describes normal-mode relaxation (subscript n) and scales with the molar concentrations of the macrodipoles, n_1 and n_2. The second term quantifies segmental relaxation (subscript s) and is proportional to the total number of segmental dipoles (i.e., the monomers). Functions f_1, f_2, and g dictate the frequency response of species 1 and 2 and the segments, respectively.

For a random-coil polymer the square of the chain dipole moment is proportional to the polymer molecular weight.[34] Equation 7 can thus be rewritten as

$$\Delta\tilde{\epsilon} = \frac{\xi'_{\mathrm{n}}}{kT}(c_1f_1(j\omega\lambda_1) + c_2f_2(j\omega\lambda_2)) + (c_1 + c_2)\frac{\xi'_{\mathrm{s}}}{kT}g(j\omega\lambda_{\mathrm{s}}) \quad (8)$$

where ξ'_{n} and ξ'_{s} are new constants, incorporating the ratio of the square of the segmental dipole moment to the segment molecular weight, and c_1 and c_2 are the mass concentrations of species 1 and 2, respectively. From eq 8 ϵ'' can be obtained as

$$\epsilon'' = \frac{\xi'_{\mathrm{n}}}{kT}(c_1 \,\mathrm{Im}\,\{f_1(j\omega\lambda_1)\} + c_2 \,\mathrm{Im}\,\{f_2(j\omega\lambda_2)\}) + (c_1 + c_2)\frac{\xi'_{\mathrm{s}}}{kT}\mathrm{Im}\,\{g(j\omega\lambda_{\mathrm{s}})\} \quad (9)$$

where Im { } is the imaginary operator. Functions Im $\{f_1\}$, Im $\{f_2\}$, and Im $\{g\}$ all decay to zero for $\omega\lambda_i \ll 1$ and $\omega\lambda_i \gg 1$.

According to eq 8, a small imbalance in the relative population of the two species, say δc_1, will distort the spectrum by the frequency-dependent amount

$$\delta(\Delta\tilde{\epsilon}) = \frac{\xi'}{kT}(f_1(j\omega\lambda_1) - f_2(j\omega\lambda_2))\delta c_1 \quad (10)$$

where we have used the condition $\delta c_2 = -\delta c_1$, reflecting the constraint of the constant total density. (We have ignored the dependence of λ_i on c_i, which is reasonable for small δc_1.) If we assume $\lambda_2 \gg \lambda_1 \gg \lambda_{\mathrm{s}}$, then $\omega\lambda_2 \gg \omega\lambda_1 \gg \omega\lambda_{\mathrm{s}}$ implies $f_1(j\omega\lambda_1) \gg f_2(j\omega\lambda_2)$ and $f_1(j\omega\lambda_1) \gg g(j\omega\lambda_{\mathrm{s}})$. Under these conditions, for $\delta c_1 > 0$, and in the region of dominance of f_1, the normal-mode spectrum will be amplified by the following factor:

$$\alpha = 1 + \frac{(f_1 - f_2)}{(f_1c_1 + f_2c_2)}\delta c_1 \cong 1 + \frac{\delta c_1}{c_1}; \quad \text{for } f_1 \gg f_2 \quad (11)$$

Therefore, the vertical shift of the spectra of Figure 10 can be explained in terms of the loss of long chains from the near-wall region.

With a minor modification, the above analysis can also be used to explain the distortion of the spectra in Figures 11 and 12. This requires incorporation in eq 8 of a "dilute" third component (i.e., the excess) with relaxation time λ_3, intermediate between λ_1 and λ_{s}. For $c_3 \ll c_1$, the third peak will cause only a minor distortion of the spectrum around $\omega \sim 1/\lambda_3$, leaving the above results unchanged. Note that there is no segmental contribution in eq 10, because the intensity of the segmental peak remains unchanged with composition.

Comparison of eqs 9 and 11 with eq 6 suggests that the factor $\alpha(t) - 1$ should be proportional to the fractional increment in the weight (or volume) fraction of the chains of intermediate size (corresponding to the dominant normal mode). Therefore, the decay of the signal back to equilibrium observed in Figure 10 could reflect the reequilibration by chain diffusion of the melt composition within the dielectric control volume. This region is defined by the total sensing area (~0.50 cm^2) and the penetration depth of the electric field, δ. The decay should then be exponential, with a time constant $\tau \approx \delta^2/(4D)$, where D is the diffusion coefficient of the chains.[47] The penetration depth of a periodic array of line sources and sinks is $\delta = L/\pi$, where L is the line spacing (see the appendix). For our sensor L = 25 μm and δ = 7.96 μm. Figure 13 gives a semilog plot of function $\alpha(t) = 1$ obtained from the data of Figure 10. The points follow the exponential fit closely, with a time constant of 34.3 h. From the relation $\tau = \delta^2/(4D)$, with $\tau = 1.23 \times 10^5$ s (34.3 h) and δ = 7.96 μm, we calculate $D = 1.28 \times 10^{-12}$ cm^2/s, which is of the correct magnitude expected for polymers in the melt. Therefore, our interpretation is consistent with both the inception-of-flow and the relaxation data.

According to the diffusional reequilibration hypothesis, the decay of the maxima in Figure 12 (quantified by the function $\beta(t)$) should also follow an exponential. In this case, the relaxation rate should be faster than that of the dominant normal mode (i.e., $\alpha(t) - 1$), given the higher relaxation frequency of these peaks (~9 kHz), characteristic of chains of lower molecular weight. Indeed, the plot of $\beta(t)$ in Figure 13 is much steeper than that of $\alpha(t) - 1$. Also, again good agreement is found with the exponential fit, even though the scatter here is somewhat higher than that of the top data. The time constant of the fit is 8.99 h, which gives a diffusion coefficient of 4.89×10^{-12} cm^2/s. This finding further substantiates the hypothesis of reequilibration by diffusion.

Other Possible Applications of the Technique. The potential of our technique transcends the specific application discussed in this paper. Novel microfabrication tools such as electron-beam, scanning-tip, and liquid-metal ion-beam lithography offer the exciting new possibility to produce miniaturized sensors with features of a size comparable to that of a polymer molecule. Microsensors and type-A polymers can then be forged into an extremely powerful tool to probe chain relaxation dynamics in systems not amenable to ordinary analytical methods.

For example, miniaturized sensors could be employed to explore the behavior of polymer chains flowing around sharp corners or to probe anisotropic relaxation in mesophases of rodlike macrodipoles.

Measurement of diffusion coefficients of macrodipoles in melts and concentrated solutions is another possible application. Calibration with polymers of known diffusivity could avoid the cumbersome task of determining the effective penetration depth of the field. The time scale of the experiment could be tailored by using sensors with different line spacings. One of the most challenging experimental problems to date has been the measurement of chain relaxation in "brushes" of polymers tethered to a solid surface. Ordinary bulk-sensitive methods are inadequate for this purpose, due to the two-dimensional nature of these structures. Dielectric microsensors could be used to measure relaxation in brushes of macro-dipoles. The penetration depth of the electric field on the sensor scales with the distance between the lines. Therefore, the surface-to-volume ratio of the device can be increased tremendously by miniaturizing the electrodes. Sensors with line spacings as small as 500 Å can now be fabricated by electron-beam lithography (at the experimental level). This length scale is comparable to that of a polymer molecule, and thus measurement of main-chain relaxation in brushes of macrodipoles will be possible with unprecedented resolution.

Conclusion

We have introduced normal-mode microdielectrometry as a new tool to probe chain relaxation in the proximity of a solid surface. We have also proposed other possible applications of this new technique to study main-chain relaxation dynamics in liquid crystal polymers and at polymer–nonpolymer interfaces.

In this work we have presented preliminary studies of flow-induced fractionation in melts of *cis*-polyisoprene undergoing plane Poiseuille flow. Analysis of the dielectric spectra of the flowing polymer revealed an increased population of fast-relaxing species near the sensor surface, indicative of the gradual buildup of a layer of low molar mass chains near the wall. The early stages of the transient could be explained by an advective mechanism, but at longer times the signal showed a complex behavior, with an overshoot before the approach to an apparent steady state. To rationalize this phenomenon, we hypothesized a transient redistribution of the molecular weight of the segregating species. This speculation will be tested in greater detail with sensors of different line spacings and mixtures of polymers with narrow molecular weight distribution.

After cessation of flow the dielectric spectra slowly relaxed back to their equilibrium shape. The exponential character of the relaxation and the magnitude of the calculated diffusivities were consistent with a reequilibration by diffusion of the melt composition within the dielectric control volume. Calculations based on a crude (but simple) model supported these hypotheses.

We believe that the present results bear nontrivial implications for modeling the flow of realistic polymeric liquids. Clearly, much more work will be required in this area before a thorough understanding of the fluid dynamics of polymer melts and solutions can be achieved.

Acknowledgment is made to the University of Notre Dame and to the donors of the Petroleum Research Fund, administered by the American Chemical Society, for support of this research. Helpful suggestions by Professor G. Marrucci for improvement of an early version of this manuscript are gratefully acknowledged. We also thank Dr. G. Bernstein of the Notre Dame Microfabrication Laboratory for helping with the SEM photographs and for informative discussions about new microfabrication techniques. J.F. expresses his gratitude to the Amoco Foundation for support through a Graduate Fellowship. Finally, we thank two anonymous reviewers for their constructive criticism.

Appendix

In this section we outline the calculation of the electric field on the dielectric sensor. Our model is a two-dimensional and periodic array of line sources and sinks of equal strength, spaced a distance L apart from each other. The electrostatic potential, $\Phi(x,y)$, and the stream function, $\Psi(x,y)$, satisfy Laplace's equation[40]

$$\nabla^2\Phi = 0; \quad \nabla^2\Psi = 0 \qquad \text{(A1)}$$

and the components of the electric field (E_x, E_y) can be obtained from

$$E_x = -\frac{\partial\Phi}{\partial x} = -\frac{\partial\Psi}{\partial y}; \quad E_y = -\frac{\partial\Phi}{\partial y} = \frac{\partial\Psi}{\partial x} \qquad \text{(A2)}$$

This problem can be solved by analogy with two-dimensional irrotational flow of an inviscid fluid.[40] A complex potential $W(z)$ is defined as

$$W(z) = \Phi(z) + j\Psi(z) \qquad \text{(A3)}$$

where $j^2 = -1$ and $z = x + jy$. For a periodic array of line sources with spacing a placed along (and orthogonal to) the y axis (Figure 3) the potential is[40]

$$W(z) = C \ln\left(\sinh\left(\pi z/a\right)\right) \qquad \text{(A4)}$$

where C is a positive constant. From eq A4 the potential and stream functions are calculated as

$$\Phi = \frac{1}{2}C \ln\left(\frac{1}{2}\left(\cosh\left(\frac{2\pi x}{a}\right) - \cos\left(\frac{2\pi y}{a}\right)\right)\right) \qquad \text{(A5)}$$

$$\Psi = C \tan^{-1}\left(\frac{\tan\left(\frac{\pi y}{a}\right)}{\tanh\left(\frac{\pi x}{a}\right)}\right) \qquad \text{(A6)}$$

Because of the linearity of the field equations, the solution for alternating sinks and sources can be obtained as a superposition of the individual solutions for the sources ($+C$) and the sinks ($-C$). This is accomplished by summing the potentials of the sinks and sources, each appropriately shifted along the y axis to produce the desired configuration. We obtain

$$\Phi = \frac{1}{2}C \ln\left(\frac{\left(\cosh\left(\frac{2\pi x}{a}\right) - \cos\left(\frac{2\pi(y - a/4)}{a}\right)\right)}{\left(\cosh\left(\frac{2\pi x}{a}\right) - \cos\left(\frac{2\pi(y + a/4)}{a}\right)\right)}\right) \tag{A7}$$

$$\Psi = C\left(\tan^{-1}\left(\frac{\tan\left(\frac{\pi(y - a/4)}{a}\right)}{\tanh\left(\frac{2\pi x}{a}\right)}\right) - \tan^{-1}\left(\frac{\tan\left(\frac{\pi(y + a/4)}{a}\right)}{\tanh\left(\frac{2\pi x}{a}\right)}\right)\right) \tag{A8}$$

Partial differentiation of these equations according to eqs A2 gives the components of the electric field E_x and E_y. Note that the positive and negative lines are now spaced a distance $L = a/2$ apart.

The complete formulas for E_x and E_y will not be given here. Instead, we shall focus on the field distribution along the lines $y = a/4$ and $y = 0$, where E_x and E_y respectively achieve their maxima. We are interested in obtaining an upper bound for the field penetration depth. We obtain

$$E_x(x,y=L/2) = -E_y^{\max} \frac{\sinh(\pi x/L)}{(\cosh^2(\pi x/L) - 1)} \tag{A9}$$

$$E_y(x,y=0) = E_y^{\max} \frac{1}{\cosh(\pi x/L)} \tag{A10}$$

where $E_y^{\max} = \pi C/L$. It is easily verified that for $x \to \infty$ E_x and E_y both approach zero and that for $x \to 0$ $E_y(x,0) \to \pi C/L$, but $E_x(x,L/2) \to \infty$. The unrealistic behavior of E_x can be avoided by considering eq A9 to be applicable everywhere except in the interior of all circular cylinders of radius R surrounding the line singularities. For $R/L \ll 1$, the cylinders are also surfaces of constant potential. Therefore, the above solution also describes the field surrounding a periodic array of metallic wires of radius R spaced a distance L apart. This configuration should approximate reasonably the electric field on our dielectric sensors.

An effective penetration depth of the field can be estimated as follows. Our technique measures a control-volume-averaged dielectric constant. The local dielectric permittivity of a polymer is a linear function of the density of dipoles.[33,38] Therefore, changes in the measured dielectric constant reflect changes in the energy-density-averaged concentration of dipoles in the dielectric control volume[48]

$$\bar{C} = \frac{1}{V}\int_0^\infty C(\vec{r})\left(\frac{|\vec{E}|(\vec{r})}{E^{\max}}\right)^2 \mathrm{d}r^3 \tag{A11}$$

where $V = A\delta$, A being the sensing area. In view of the crudeness of our model, detailed calculations with eq A11 and the full electric field are not warranted. For simplicity, we assume that $|E|(r)/E^{\max} = E_y(x,0)/E_y^{\max}$ and $C(r) =$ constant, giving the following estimate for the penetration depth, δ:

$$\delta = \int_0^\infty \left(\frac{E_y(x,y=0)}{E_y^{\max}}\right)^2 \mathrm{d}x = \frac{2L}{\pi}\left[\frac{-1}{(1 + \exp(2\pi x/L))}\right]_0^\infty = \frac{L}{\pi} \tag{A12}$$

Equation A12 gives an upper bound for δ. A more detailed analysis (accounting for our specific sensor geometry and the glass substrate) is being currently worked out and will be presented in a future work.

References and Notes

(1) Wu, S. *Polymer Interface and Adhesion*; Dekker: New York, 1982.
(2) Alperin, A.; Tirrel, M.; Lodge, T. P. *Adv. Polym. Sci.* **1991**, *100*.
(3) Denn, M. M. *Annu. Rev. Fluid Mech.* **1990**, *22*, 13.
(4) Cohen, Y.; Metzner, A. B. *J. Rheol.* **1985**, *29*, 67.
(5) Cohen, Y.; Metzner, A. B. *AIChE Symp. Ser.* **1982**, *78* (No. 212), 77.
(6) Cohen, Y.; Metzner, A. B.; Rangel-Nafaîle, C. *J. Non-Newtonian Fluid. Mech.* **1979**, *5*, 449.
(7) Chung, C. I. *Trans. N.Y. Acad. Sci.* **1974**, *36*, 311.
(8) Busse, W. F. *Phys. Today* **1964**, *17*, 32.
(9) Schreiber, H. P.; Storey, S. H. *J. Polym. Sci.* **1965**, *B3*, 723.
(10) Schreiber, H. P.; Storey, S. H.; Bagley, E. B. *Trans. Soc. Rheol.* **1966**, *10* (1), 275.
(11) Schreiber, H. P. *J. Appl. Polym. Sci.* **1974**, *18*, 2501.
(12) Hedvig, P. *Dielectric Spectroscopy of Polymers*; Wiley: New York (printed in Hungary), 1975.
(13) Bartnikas, G., Eichhorn, L. V., Eds. *Engineering Dielectrics*; ASTM Special Technical Publication 783; ASTM: Baltimore, MD, 1983; Vol. IIA.
(14) Kranbuehl, D. E.; Delos, S. E.; Jue, P. K. *Polymer* **1986**, *267*, 11.
(15) Gotro, J.; Yandrasits, M. *Polym. Eng. Sci.* **1989**, *29* (5), 278.
(16) Senturia, S.; Gaverick, S. U.S. Patent 4,423,371.
(17) Kranbuehl, D.; Delos, M.; Haverty, P. *Polym. Eng. Sci.* **1989**, *29* (5), 285.
(18) von Hippel, A. R., Ed. *Dielectric Materials and Applications*; MIT Press and Wiley: New York, 1954.
(19) Pae, K. D. *J. Polym. Sci.* **1983**, *21*, 1195.
(20) Blundell, K. D.; Buckingham, K. A. *Polymer* **1985**, *26*, 1623.
(21) Takase, Y.; Mitchell, G. R.; Odajima, A. *Polym. Commun.* **1986**, *27*, 76.
(22) Alhaj-Mohammed, M. H.; Davies, G. R.; Abdul Jawad, S.; Ward, I. M. *J. Polym. Sci., Polym. Phys. Ed.* **1988**, *26*, 1751.
(23) Gedde, U. W.; Buerger, D.; Boyd, R. H. *Macromolecules* **1987**, *20*, 988.
(24) Bormuth, F. J.; Haase, W. *Mol. Cryst. Liq. Cryst.* **1987**, *153*, 207.
(25) Haws, C. M.; Clark, M. G.; McArdle, C. B. *Mol. Cryst. Liq. Cryst.* **1987**, *153*, 537.
(26) Bur, A. J.; Roberts, D. E. *J. Chem. Phys.* **1969**, *51* (1), 406.
(27) Williams, G. *J. Polym. Sci., Polym. Phys. Ed.* **1983**, *21*, 2037.
(28) Moscicki, J. K.; Williams, G. *J. Polym. Sci., Polym. Phys. Ed.* **1983**, *21*, 197.
(29) Wada, A. *J. Chem. Phys.* **1959**, *31* (2), 495.
(30) Stockmayer, W. H. *Pure Appl. Chem.* **1967**, *15*, 247.
(31) Adachi, K.; Kotaka, T. *Macromolecules* **1984**, *17*, 120.
(32) Adachi, K.; Kotaka, T. *Macromolecules* **1985**, *18*, 466.
(33) Adachi, K.; Kotaka, T. *Macromolecules* **1988**, *21*, 157.
(34) Imanishi, Y.; Adachi, K.; Kotaka, T. *J. Chem. Phys.* **1988**, *89* (12), 7585.
(35) Adachi, K.; Yoshida, H.; Fukui, F.; Kotaka, T. *Macromolecules* **1990**, *23*, 3138.
(36) Boese, D.; Kremer, F. *Macromolecules* **1990**, *23*, 829.
(37) Bird, R. B.; Hassager, O.; Armstrong, R. C.; Curtiss, C. F. *Dynamics of Polymeric Liquids*, 2nd ed.; Wiley: New York, 1987; Vols. 1 and 2.
(38) Doi, M.; Edwards, S. F. *The Theory of Polymer Dynamics*; Oxford University Press: New York, 1989.
(39) Larson, R. G. *Constitutive Equations for Polymer Melts and Solutions*; Butterworth: Stoneham, MA, 1988.
(40) Lamb, H. *Hydrodynamics*; Cambridge University Press: Cambridge, U.K., 1932.
(41) Vogel, H. *Z. Phys.* **1921**, *22*, 645.
(42) Fulcher, G. S. *J. Am. Ceram. Soc.* **1925**, *8*, 339.
(43) Tamman, G.; Hesse, W. *Z. Anorg. Allg. Chem.* **1926**, *156*, 245.
(44) Havriliak, S.; Negami, S. *J. Polym. Sci., Part C* **1966**, *14*, 99.
(45) Havriliak, S.; Negami, S. *Polymer* **1967**, *8*, 161.
(46) Zimm, B. H. *J. Chem. Phys.* **1956**, *24*, 269.
(47) Bird, R. B.; Stewart, W. E.; Lightfoot, E. N. *Transport Phenomena*; Wiley: New York, 1960.
(48) Prager, S.; Kunkin, W.; Frisch, H. L. *J. Chem. Phys.* **1970**, *52* (10), 4925.

Registry No. PI (homopolymer), 9003-31-0.